ACS OMEGA

Open Access

http://pubs.acs.org/journal/acsodf

Article

Influence of Controlled Dipolar Interaction for Polymer-Coated Gd-Doped Magnetite Nanoparticles toward Magnetic Hyperthermia Application

Krishna Priya Hazarika, C. Borgohain, and J. P. Borah*

Cite This: *ACS Omega* 2024, 9, 6696−6708

Read Online

ACCESS | Metrics & More | Article Recommendations | Supporting Information

ABSTRACT: To maximize heat release from immobilized nanoparticles (NPs), a detailed understanding of the controlled dipolar interaction is essential for challenging magnetic hyperthermia (MH) therapies. To design optimal MH experiments, it is necessary to precisely determine magnetic states impacted by the inevitable concurrence of magnetic interactions under a common experimental form. In this work, we describe how the presence of dipolar interaction significantly alters the heating mechanism of host materials when NPs are embedded in them for MH applications. The concentration of the NPs and the intensity of their interaction can profoundly impact the amplitude and shape of the heating curves of the host material. The heating capability of interacting NPs might be enhanced or diminished, depending on their concentration within the host material. We propose chitosan- and dextran-coated Gd-doped Fe_3O_4 NPs directing dipole interactions effective for the linear regime to enlighten the pragmatic trends. The outcomes of our study may have substantial implications for cancer therapy and could inspire novel approaches for maximizing the effectiveness of MH.

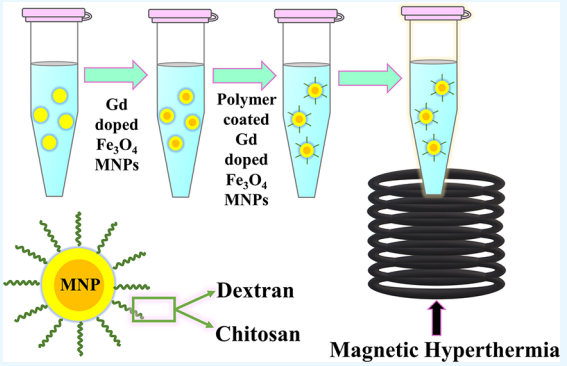

1. INTRODUCTION

Magnetic nanoparticles (MNPs) have been one of the most predominant nanomaterials in recent decades, as their versatile characteristics allow for a inclusive range of appliances in the areas like biomedicine, electronics, technology, and energy.[1−3] In magnetic fluid hyperthermia (MFH), MNPs gained significant attention due to its potential applications as a thermal therapy in cancer trials, and thermally triggered drug delivery under alternating magnetic field.[4] For clinically available hyperthermia, improved magnetic anisotropy, controlling magnetic domain size, and interparticle dipole interactions are the key parameters for enhancing the effective heating efficiency.[5]

Although several challenges hinder the development of these nanomaterials, an example is the instability of oxidation states of the Fe_3O_4 (FO) MNPs, which affects the magnetic tuning, structure, and optimum self-heating efficiency for MFH application.[6,7] Much effort has been devoted to emerging synthesis approaches to control particle size and other parameters to enhance the particle intrinsic heating efficacy to date. Researchers have drawn significant interest in rare earth (RE) ions due to the *f*-block arrangement and their exceptional optical and magnetic states, which have demonstrated that adding such dopants in the FO system profoundly impacts the final product.[2,8−12] Several studies have been conducted to improve the saturation magnetization; Slimani et al. reported the same results for the influence of Sm^{3+} and Er^{3+} doping on the $CoFe_2O_4$ system.[13]

Moreover, another challenge is the dispersion of MNPs in aqueous solutions. Since MNPs have high surface energies, they are prone to agglomerate. Thus, to fully demonstrate the functions of MNPs, it is essential to work on technologies to prevent aggregation and agglomeration and to increase their dispersibility. One of the most popular methods for agglomeration control is via the effective conjugation of biomolecules, such as peptides, oligonucleotides, antibodies, and natural polymers. Although MNPs with enhanced functionalities/dispersibility or specific absorption rate (SAR) have been attained, obtaining MNPs with both functionalities/dispersibility and high SAR is still a challenge to overcome. Among these, dextran- and chitosan-coated Fe_3O_4 MNPs are particularly notable due to the fact that they are nonantigenic, biocompatible, biofunctional, and biodegradable, and standing as an exceptional candidate for clinical trials for hyperthermia application. Recently, much research has been conducted to

Received: October 8, 2023
Revised: November 1, 2023
Accepted: November 9, 2023
Published: February 1, 2024

improve ferrite NPs' dispersibility and control agglomeration by using dextran and chitosan biopolymers.[14−16] Interestingly, dextran is an FDA-approved biopolymer, and dextran-coated iron oxide NPs are known as Feridex, which have been ratified for MRI contrast agents.[17] However, chitosan is a natural polymer composed of glucosamine and N-acetyle-D-glucosamine and has been widely exploited for biomedical applications owing to their biocompatible, biodegradable, and bioactive properties.[15] In particular, chitosan enhances the colloidal stability of MNPs and in vivo blood circulation.[18]

Henceforth, a strong demand exists for methods that produce MNPs via clear, colloidally stable, simple, and efficient contenders for magnetic hyperthermia (MH) application. The study is a continuation of our prior work, where we explored the role of Gd doping on Fe_3O_4 MNPs to tune heating efficiency.[9] Herein, with the aim of emerging an ideal nanotherapeutic agent that behaves as highly stable in physiological atmospheres, a dextran-coated Gd-doped Fe_3O_4 (DGFO) and chitosan-coated Gd-doped Fe_3O_4 (CGFO) system (Figure 1) have been synthesized.

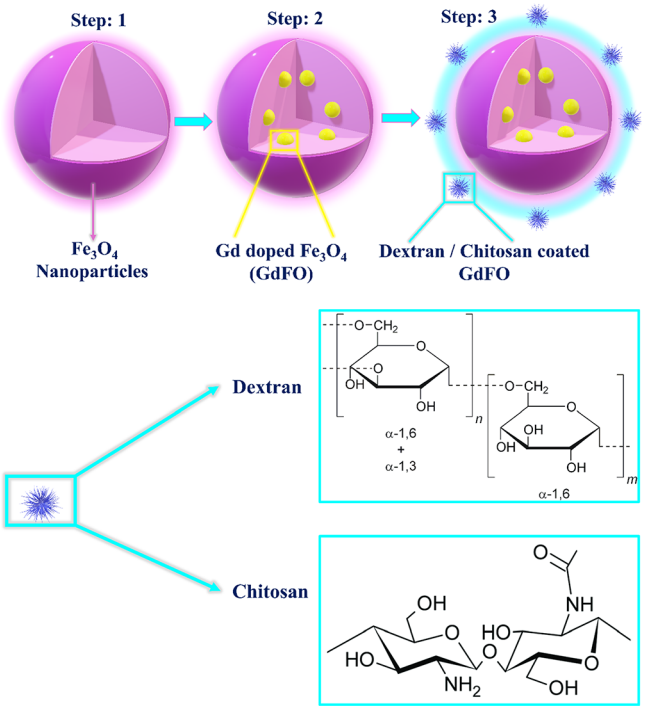

Figure 1. Schematic of dextran- and chitosan-coated Gd-doped Fe_3O_4 MNPs.

2. MATERIALS AND EXPERIMENTAL TECHNIQUE

2.1. Preparation of the MNPs. The comprehensive route for preparing the Gd-doped Fe_3O_4 (GdFO) MNPs is exemplified in our prior work.[9] Therefore, we worked on the 7% Gd-doped Fe_3O_4 system for the capture of dextran and chitosan. Here, we report the concise expression of the synthesizing procedure for dextran- and chitosan-coated Gd-doped Fe_3O_4 MNPs only.

2.1.1. Preparation of GdFO MNPs. Fe_3O_4 NPs had processed through a standard coprecipitation route. Briefly, a homogeneous solution was formed by dissolving $FeCl_3$ (ferric chloride) and $FeCl_2$ (ferrous chloride) in 100 mL of hydrazine mixed double-deionized water. The prepared composition was stirred for 1 h 30 min, and NaOH solution was added dropwise to maintain the pH 7−8. The prepared composition was kept for cooling, after which the sample was washed with ethanol and Milli-Q (double-deionized) water and centrifuged at 2000 rpm. A black precipitate was attained, then dehydrated in a vacuum oven at 90 °C for 11 h, and finally pulverized to powder.

2.1.2. Preparation of CGdFO/DGdFO MNPs. All designed MNPs were prepared via the coprecipitation route, and the obtained GdFO is further functionalized using biopolymers, dextran, and chitosan, abbreviated as DGdFO and CGdFO throughout the manuscript. In the experimental system, 0.25 g of chitosan was dissolved in 100 mL of 0.1 M acetic acid solution and was added dropwise to 0.5 g of GdFO, prepared in 10 mL of double-deionized water under constant stirring at 180 rpm for 20 min, and then ultrasonicated for 20 min. Then, the processed MNPs were washed with ethanol and centrifuged at 2000 rpm for 15 min. The precipitate attained from the experiments was dehydrated in a vacuum oven and last hand-milled to powder. Similarly, the same procedure was followed for preparing DGdFO MNPs. Herein, dextran was directly dissolved in double-deionized water instead of 0.1 M acetic acid solution, as shown in Figure 2.

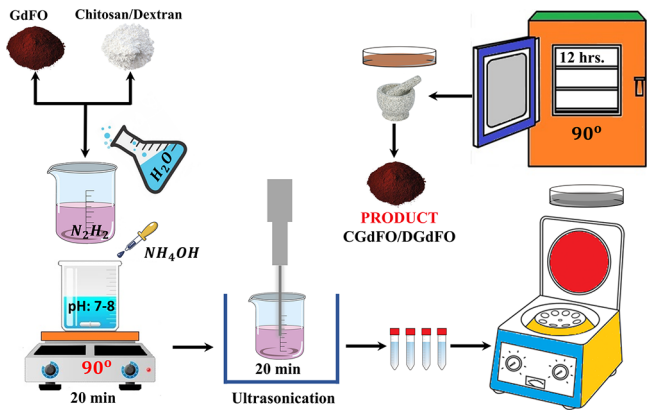

Figure 2. Synthesis scheme of processed MNPs.

2.2. Characterization. The crystallographic statistics and phase information on the reference MNPs were studied via X-ray diffraction (Rigaku, Ultima IV) with Cu−Kα radiation (λ = 1.5406 Å). States of the elements and functional groups were investigated via Fourier transform infrared spectra (FTIR) (Cary 630, Agilent Technology). The morphology, average particle size, alongside selected area electron diffraction (SAED), and *d*-spacing were examined through a scanning electron microscope (FESEM; ZEISS, Gemini 300) and a high-resolution transmission electron microscope (TEM; JEOL, JEM 2100), respectively. Furthermore, a detailed investigation of the electronic and chemical states of the MNPs was investigated by X-ray photoelectron spectroscopy (XPS) (Thermo Fisher Scientific, Excalab Xi$^+$ with Al Kα as the source of X-ray). Using a Hitachi STA7300 thermal analyzer, a thermogravimetric study (TGA) was carried out from room temperature to 800 °C under the N_2 atmosphere. The magnetic behavior of the MNPs was examined using a vibrating sample magnetometer (VSM; Lakeshore, 7410 series) and electron spin resonance (ESR) techniques (JEOL, JES-FA200). The processed samples are subjected to

https://doi.org/10.1021/acsomega.3c07835
ACS Omega 2024, 9, 6696−6708

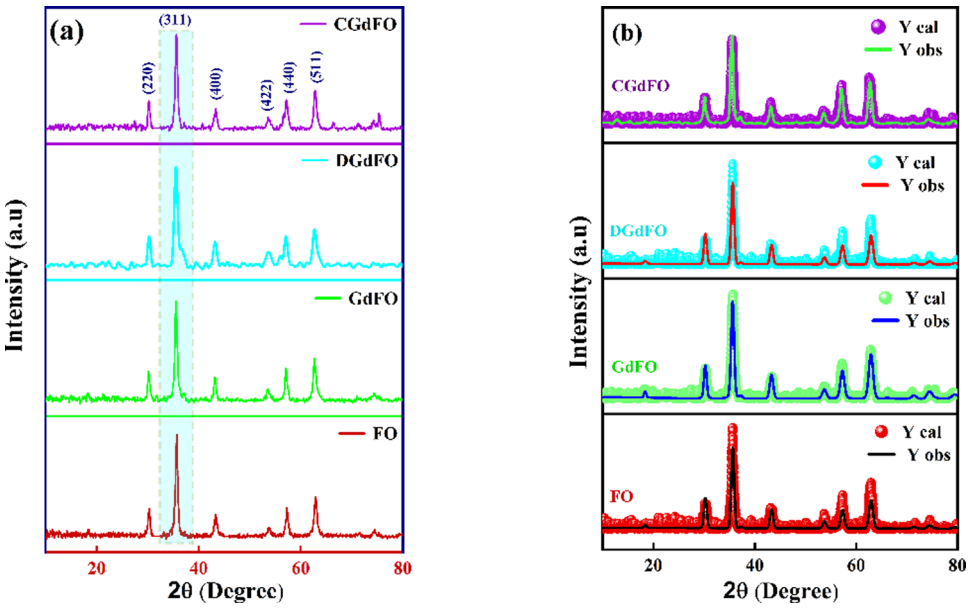

Figure 3. (a) XRD patterns of processed MNPs. (b) RR of the processed MNPs

Table 1. Distribution of Cation from RR and Structure Parameters (Crystallite Size, U Parameter, Tetrahedral Radius R_A, Octahedral Radius R_B, Bond Lengths (A−O and B−O), Strain (ε), and Cell Volume)

sample name	FO	GdFO	DGdFO	CGdFO
cation distribution	$Fe^{3+}[[Fe]^{2+}Fe^{3+}]O_2$	$\delta = 0$ $[Fe^{3+}_{0.989}]_A$ $[[Gd]^{3+}_{0.667}Fe^{2+}_{0.276}Fe^{3+}_{1.056}]O_4$	$\delta = 0.045$ $[Gd^{3+}_{0.576}Fe^{3+}_{0.424}]_A[Gd^{3+}_{0.168}Fe^{2+}_{0.293}Fe^{3+}_{1.371}]_BO_4$	$\delta = 0.045$ $[Gd^{3+}_{0.691}Fe^{3+}_{0.309}]_A[Gd^{3+}_{0.269}Fe^{2+}_{0.279}Fe^{3+}_{1.452}]_BO_4$
crystallite size (nm)	13.23	15.06	17.32	17.11
particle size D_{TEM} (nm)	15 ± 3	16 ± 3	18 ± 3	17 ± 2
U	0.25	0.25	0.26	0.26
r_A (Å)	1.86	1.86	1.87	1.88
r_B (Å)	2.04	2.06	2.07	2.08
A−O (Å)	0.06	0.06	0.08	0.08
B−O (Å)	3.09	3.11	3.14	3.17
ε	0.004	0.006	0.007	0.005
cell volume (Å)	581.71	582.28	582.37	582.47

a self-heating study using an induction heating setup (Easy Heat-8310, Ambrell make, UK).

3. RESULTS AND DISCUSSION

3.1. Structure and Morphology Study. The powder XRD scans of designed dextran- and chitosan-coated Gd-doped Fe_3O_4 MNPS are portrayed in Figure 3a. The experimental XRD peak positions fit competently with the magnetite phase[19] and show the high crystallinity of these MNPs. Hereafter, the reflections from the atomic planes (220), (311), (400), (422), (440), and (511) correspond to the single-phase face-centered cubic spinel structure with the space group $Fd\bar{3}m$. Additionally, dextran and chitosan have a noncrystalline structure; thus, no alternation of the crystal structure was observed for DGdFO and CGdFO MNPs.[20]

Furthermore, Rietveld refinement (RR) has been carried out via Full Proof software to delve further into the structure parameter, in brief, the distribution of cations, and cell constants, as portrayed in Figure 3b.[21,22] Figure 3 depicts the fine agreement of the experimental and theoretical curves, with lower standards of various *R*-factors and Goodness-of-fit χ^2 (~2).[22] The computed parameters from RR, cation distribution, and structure parameters (crystallite size, U parameter, tetrahedral radius R_A, octahedral radius R_B, bond lengths (A−O and B−O), and cell volume) are enclosed in Table 1. It has been observed from RR analysis that functionalized dextran and chitosan appear to have influenced the cation distribution

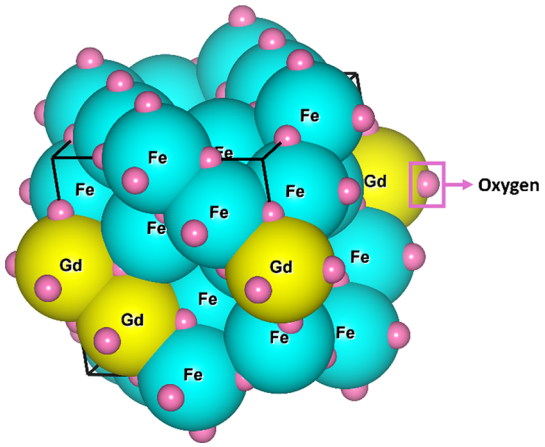

Figure 4. Space-filling representation of the *fcc* cubic spinel structure of GdFO MNPs.

https://doi.org/10.1021/acsomega.3c07835
ACS Omega 2024, 9, 6696−6708

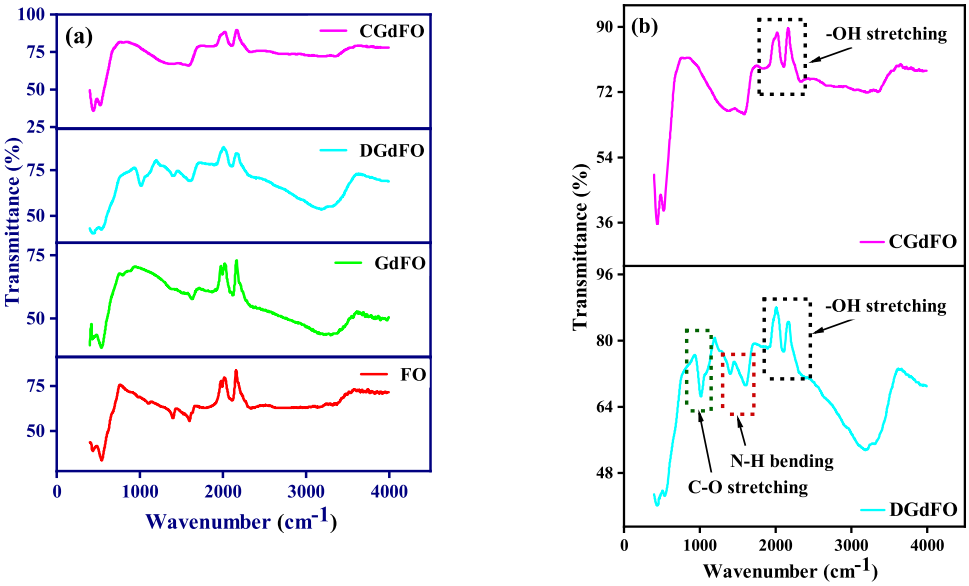

Figure 5. (a) FTIR spectra of the synthesized MNPs. (b) Detailed overview of the signature peak for CGdFO and DGdFO MNPs.

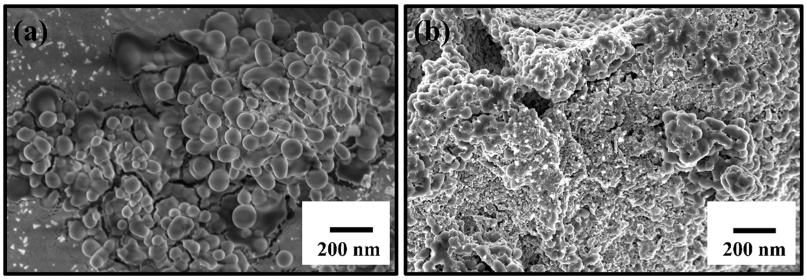

Figure 6. SEM micrographs: (a) chitosan-coated Gd-doped FO MNPs and (b) dextran-coated Gd-doped FO MNPs.

in the FO matrix. Henceforth, due to the incomplete coordination of oxygen ions, coordination symmetry can be abridged at the surface of nanoscale spinel FO systems, which further affects the magnetic properties of the processed MNPs. Moreover, Figure 4 displays the Space-filling image of the *fcc* cubic spinel structure of GdFO MNPs, generated from VESTA software, where we can visualize that before coating the Gd ions prefer to be at octahedral sides rather than tetrahedral sites of the FO matrix.

The enhancing trend for crystallite size and cell volume indicates an enlargement of average crystallite size for the developed strain. Moreover, dextran and chitosan coating in our respective ferrite matrix enriched bond lengths (A−O/B−O) as represented in Table 1. An increase in bond length may be caused by the substitution of cations, lattice strain, finite size effect, and lattice stress,[23] etc.

FTIR spectra of processed MNPs are depicted in Figure 5 around the frequency range of 400−4000 cm^{-1}. The spectrum of all the processed MNPs parades two distinct absorption bands, ∼428 and ∼540 cm^{-1}, which are in accordance with the spinel ferrite structure.[24] The absorption bands (υ_1) ∼540 cm^{-1} and (υ_2) ∼428 cm^{-1} appear due to the Fe−O stretching vibration of the tetrahedral metal complex and an octahedral metal complex, respectively.[25] Figure 5 depicts the shifting of the absorption band (υ_2) ∼428 cm^{-1} toward the higher wavenumber number side, which confirms the consequence of Gd ions on the octahedral voids of the Fe_3O_4 system, which ratifies the computed XRD results. Moreover, a broad absorption peak within ∼3450−3550 cm^{-1} has been observed, corresponding to the O−H stretching vibrations of the absorbed H_2O molecule.[26] The additional absorption peak that emerged at ∼1595 cm^{-1} and ∼1371 cm^{-1} refers to N−H bending and C−O stretching observed for CGdFO MNPs, implying the proper coating of chitosan on the surface of the processed MNPs.[15,16,26] For DGdFO spectra, the extra peak observed in the range of ∼1000 and ∼1250 cm^{-1} ascribed the presence of C−O stretching and C−O−C stretching of the polymeric chain of dextran, indicating the proficient coating of dextran on the GdFO system.[14]

Figure 6 presents the surface morphology image of the chitosan- and dextran-coated characterized MNPs. The SEM images parade grapes-like, nonuniform, and nearly spherical morphology. Herein, due to the nonmagnetic coating of the processed MNPs, the agglomeration is effectively controlled for the coated NPs compared to the bare one, which is clearly visualized from the respective SEM micrographs. Further, it supports the TEM analysis.

The TEM micrographs displayed in Figure 7 illustrate that most of the synthesized MNPs are nearly spherical, and agglomeration is effectively controlled, which is in fine accordance with the SEM results. The log-normal distribution is used to estimate the particle size of FO, GdFO, DGdFO, and CGdFO MNPs, which is highly consistent with the XRD results and enclosed in Table 1 and shown in the Supporting Information file (ESI Figure 1*). Moreover, in Figure 7, a visible increasing particle size is observed, which can be

https://doi.org/10.1021/acsomega.3c07835
ACS Omega 2024, 9, 6696−6708

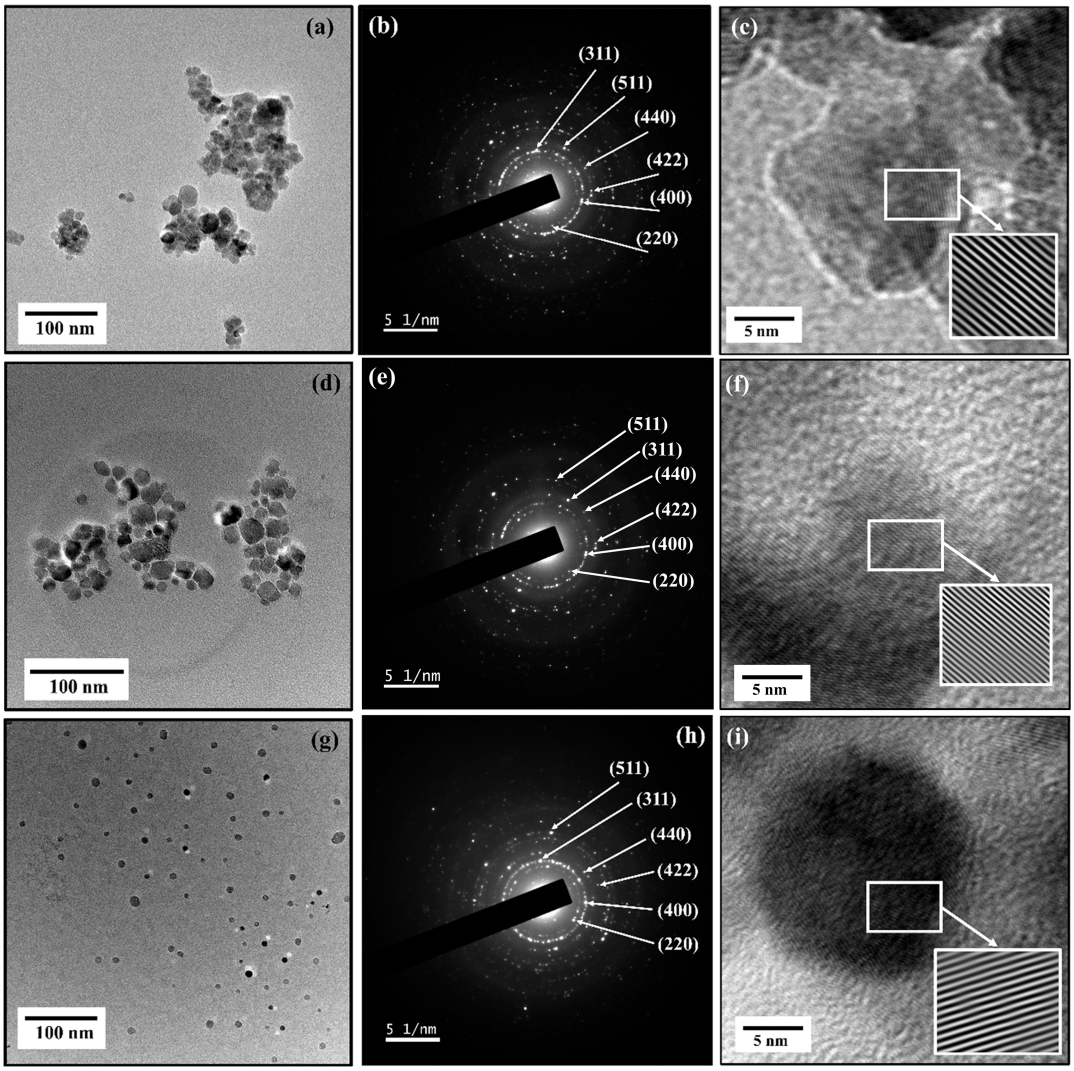

Figure 7. TEM images: (a) GdFO MNPs, (b) SAED inset of GdFO MNPs, (c) *d*-spacing of GdFO MNPs, (d) DGdFO MNPs, (e) SAED inset of DGdFO MNPs, (f) *d*-spacing of DGdFO MNPs, (g) CGdFO MNPs, (h) SAED inset of CGdFO MNPs, and (i) *d*-spacing of CGdFO MNPs.

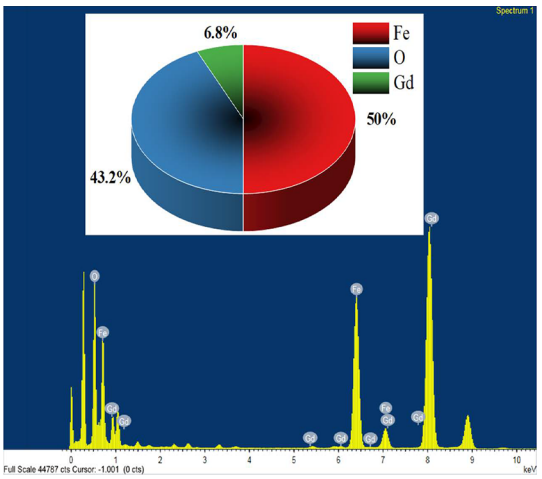

Figure 8. Elemental mapping of GdFO MNPs.

attributed to functionalized chitosan and dextran having influenced the structure and modified the particle size and shape. One possible explanation for the difference in size between the chitosan- and dextran-coated NPs is the presence of charges attributed to chitosan macromolecules that are not present in dextran. Chitosan is well-known to have high biocompatibility due to the reactive functional groups present, namely, (−OH) and amino ($-NH_2$) groups. In the presence of the positively charged amino groups of coated MNPs, the chitosan-coated NPs may be repelled from each other due to electrostatic interactions, limiting their aggregation and resulting in smaller and more isolated particles.[27] On the other hand, the absence of charges in dextran may lead to partial agglomeration of the NPs, resulting in larger particle sizes. The SAED pattern has concentric rings with spots, indicating the MNPs are polycrystalline in nature.[28] The spotty rings anticipated to the Bragg reflection planes (220), (311), (400), (422), (511), and (440), respectively, which is consistent with the XRD results. Accordingly, the *d*-spacing consistent with the (311) plane perfectly matches the XRD data.

In addition, Figure 8 depicts the elemental mapping of GdFO MNPs from EDX analysis to convey the existence of the elements Fe, Gd, and O, and Gd, respectively. The atomic % of GdFO MNPs from the elemental analysis closely matches the experimentally determined stoichiometric values.

https://doi.org/10.1021/acsomega.3c07835
ACS Omega 2024, 9, 6696−6708

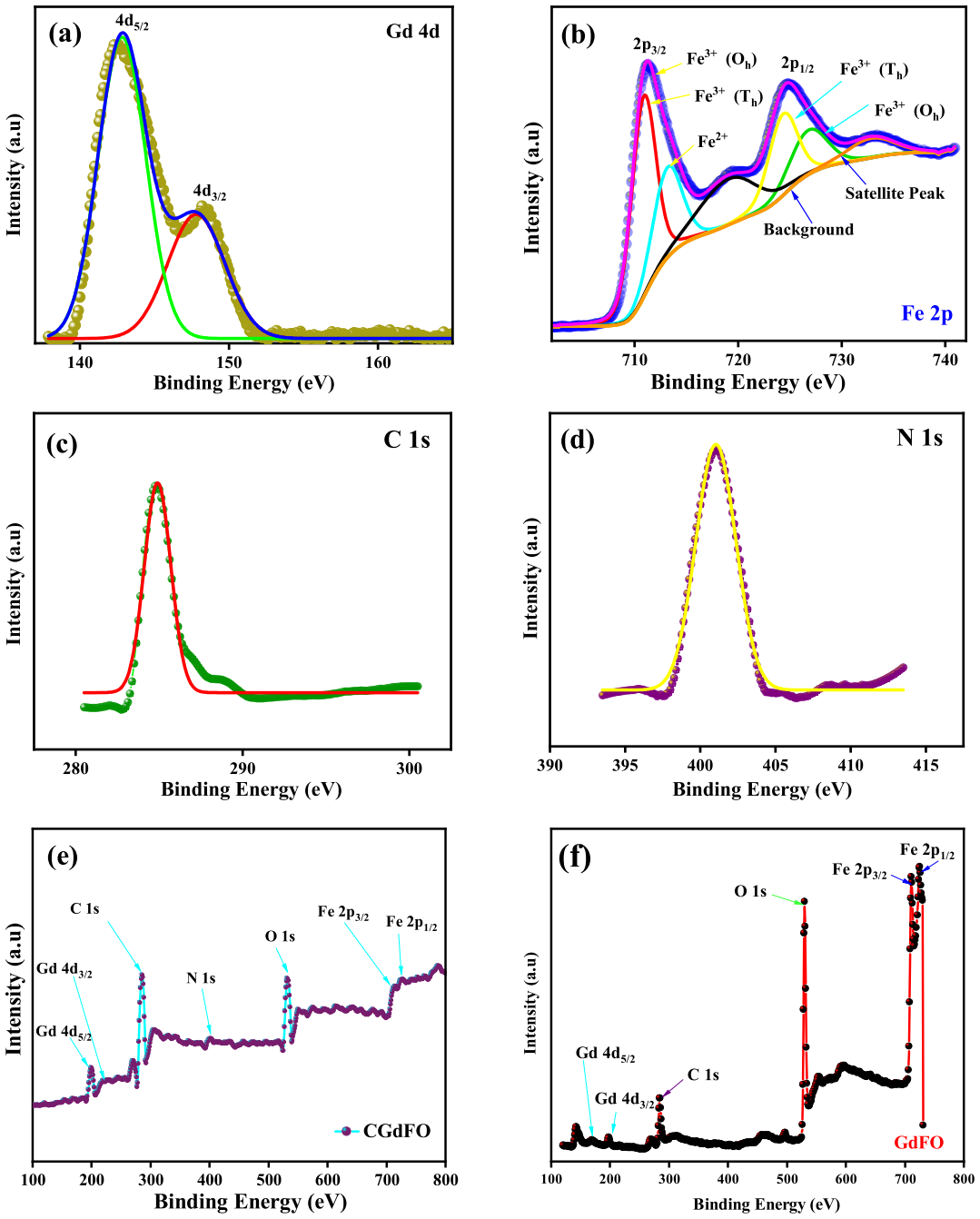

Figure 9. XPS scans of chitosan-coated Gd-doped FO (CGdFO): (a) Gd 4d spectra, (b) Fe 2p spectra, (c) C 1s spectra, (d) N 1s spectra, (e) complete survey of CGdFO MNPs, and (f) complete survey of GdFO MNPs.

The chitosan coating with Gd-doped MNPs was investigated by using XPS analysis. The binding energies of the Gd and Fe peaks can be used to determine the chemical bonding and oxidation states of the elements in the NPs. The peaks at ∼143 and ∼150 eV signify the incorporation of Gd ions in the FO system, and the peak indicates the spin−orbital characteristics of $4d_{5/2}$ and $4d_{3/2}$, respectively, as directed in Figure 9a, and the Gd exhibit 3^+ valence state. Additionally, the occupying two bonds with octahedral and tetrahedral sites can be visualized via satellite peaks of the Gd 4d scan. However, Figure 9b illustrates the core Fe 2p electron scan of the processed MNPs at high resolution, exposing the spin−orbital characteristics of $2p_{3/2}$ and $2p_{1/2}$ at the peaks ∼711 and ∼722 eV, respectively. Herein, the scan specifies that Fe ions have valence states of 2^+ and 3^+, and the satellite Fe peaks represent the bond formation initiated by octahedral (O_h) and tetrahedral sites (T_h).[9] The observed C 1s, N 1s, and O 1s spectra in Figure 9c,d, with a precise nitrogen peak at around 399 eV, confirm the presence of chitosan on the surface of the NPs. Henceforth, the complete survey scan displayed in Figure 9e shows peaks corresponding to iron, gadolinium, oxygen, carbon, and nitrogen, indicating the presence of both the Gd-doped magnetite core and the chitosan coating. The overall survey scan of GdFO MNPs, as depicted in Figure 9f, displays the successful doping of Gd in the FO matrix. The Gd and Fe peaks were shifted in the coated NPs compared to those in the uncoated NPs, indicating successful doping and coating with chitosan in the Gd-doped FO system.

https://doi.org/10.1021/acsomega.3c07835
ACS Omega 2024, 9, 6696−6708

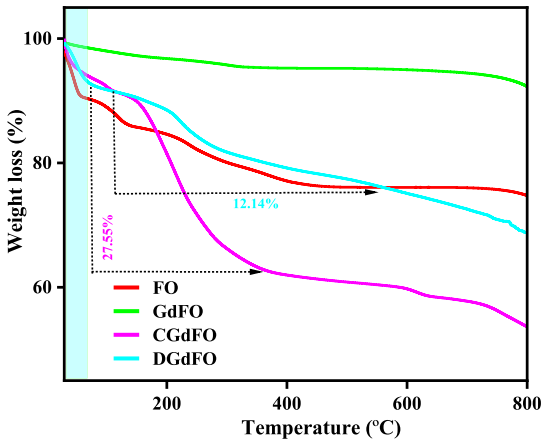

Figure 10. TGA study of the synthesized MNPs.

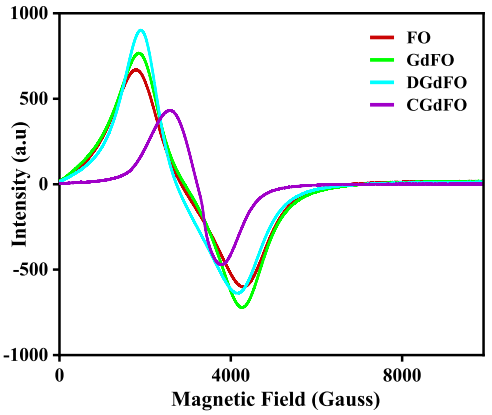

Figure 11. ESR spectra of the reference MNPs.

Table 2. Measured ESR Parameters (Spin−Spin Relaxation Time τ_1, Spin−Lattice Relaxation Time τ_2, Effective g Value, Resonance Line Width H_{pp}, FWHM of the Absorption Spectra $\Delta H_{1/2}$, and Resonance Field H_r)

sample details	$\tau_1 \times 10^{-11}$ (s)	$\tau_2 \times 10^{-12}$ (s)	g	H_{pp} (Gauss)	$\Delta H_{1/2}$ (Gauss)	H_r (Gauss)
FO	1.29	5.50	2.03	2495	4321	2706
GdFO	1.44	4.93	2.02	2251	3898	2877
DGdFO	1.47	4.85	2.02	2217	3839	2879
CGdFO	1.53	4.62	2.01	2115	3663	3210

3.2. Thermogravimetric Analysis (TGA). Thermogravimetric analysis (TGA) is being performed between room temperature and 800 °C in an N_2 atmosphere to determine the thermal stability, phase crystallinity, and the weight percentage (wt %) of chitosan and dextran at the surface of the Gd-doped Fe_3O_4 NPs. Figure 10 portrays the degradation of the watery compounds, metal hydroxides, and unreacted organic traces. The weight loss under 100 °C for all of the synthesized MNPs is ∼9%, attributed to the purging of absorbed water on the uncoated FO MNPs. Furthermore, Gd doping affects thermal stability as weight loss decreases to 5%, incorporating Gd ions in the FO matrix. In contrast, dextran- and chitosan-functionalized MNPs exhibited a considerable amount of weight loss of 12.14 and 27.55 wt %, respectively, within 150 and 600 °C, which is in good agreement with the reported previous studies.[20,29] Above 600 °C, a slow weight loss is observed in Figure 10; henceforth, only the residual of MNPs remains after the whole degradation of dextran and chitosan. Based on TGA results, the amount of dextran- and chitosan-coated on the surface of uncoated GdFO MNPs was calculated at approximately 3.14 and 18.55 wt %, respectively.

3.3. Magnetic Analysis. To analyze the magnetic parameters of the characterized MNPs, spin-related phenomena, and relaxation mechanisms, an ESR is employed, as depicted in Figure 11. A summary of the calculated ESR measurements, spin−spin relaxation time (τ_1), spin−lattice relaxation time (τ_2), the resonance field (H_r), resonance line width (H_{pp}), effective g value, and *fwhm* of the absorption spectra ($\Delta H_{1/2}$) is enclosed in Table 2. The listed H_r values follow an increasing trend due to the constant drop in the saturation magnetization and magnetic anisotropy of their internal fields and can be further established via a VSM study. Hereafter, the broad ESR graph with $g \sim 2$ implies the superparamagnetic phase of the processed MNPs.[30] Most interestingly, the broadening of the curves indicates the presence of dominating dipolar−dipolar interaction.[31] Furthermore, the small value of g and H_{pp} signifies the strong superexchange interaction. Henceforward, the lower g and H_{pp} values for dextran- and chitosan-coated Gd-doped MNPs suggest a random alignment of magnetic moments with improving particle size.[32−34]

In particular, for the MFH analysis, the SAR is a key parameter for determining the heating efficacy of the magnetic ensemble, and it relates inversely to the relaxation time. As listed in Table 2, the observed lower spin−spin relaxation time (τ_1) results in a higher SAR, as validated by induction heating analysis.[35] Additionally, spin−lattice relaxation time (τ_2) ensues the spin−orbit coupling of the characterized MNPs whereas spin−spin relaxation time (τ_1) correlates with the exchange energy among themselves.[36]

The magnetic states of processed MNPs are portrayed in Figure 12, and the performed Langevin fit of each hysteresis graph indicates the superparamagnetic nature of the NPs.[37] As part of accurately estimating saturation magnetization (M_s) and effective anisotropy (K_{eff}) constant, we have fitted the hysteresis graphs with the Law of approach to saturation magnetization (LAS).[38] The calculated magnetic parameters, viz., saturation magnetization (M_s), effective anisotropy constant (k_{eff}), retentivity (M_r), and coercivity (H_c) from the S-shaped hysteresis graphs, are listed in Table 3.

Hereafter, Figure 13 shows the comparative behavior of saturation magnetization (M_s), coercivity (H_c), and effective magnetic anisotropy (K_{eff}) of the synthesized MNPs. The comparative analysis reveals that (M_s), (H_c), and (K_{eff}) decreased for the chitosan- and dextran-coated MNPs in comparison to the bare FO and GdFO NPs. The processed GdFO exhibit lower M_s than FO MNPs due to the inflow of cations toward the octahedral site enhanced compared to bare FO MNPs and resulting increment of magnetic moment in the FO matrix.[39−41] Additionally, as observed in Table 3, the saturation magnetization (M_s) for chitosan- and dextran-coated Gd-doped magnetite NPs has decreased compared to GdFO and FO MNPs. Moreover, the RR exemplified the influence of the cation distribution for CGdFO and DGdFO. Henceforward, the decrement of M_s is basically due to the surface effects, magnetic dilution as chitosan and dextran are nonmagnetic in nature, and interfacial effects.[14,15,42,43] In this regard, the structural and magnetic states of the synthesized MNPs have a clear and direct correlation.[44] As mentioned above, according to the XRD study, chitosan and/or dextran

https://doi.org/10.1021/acsomega.3c07835
ACS Omega 2024, 9, 6696−6708

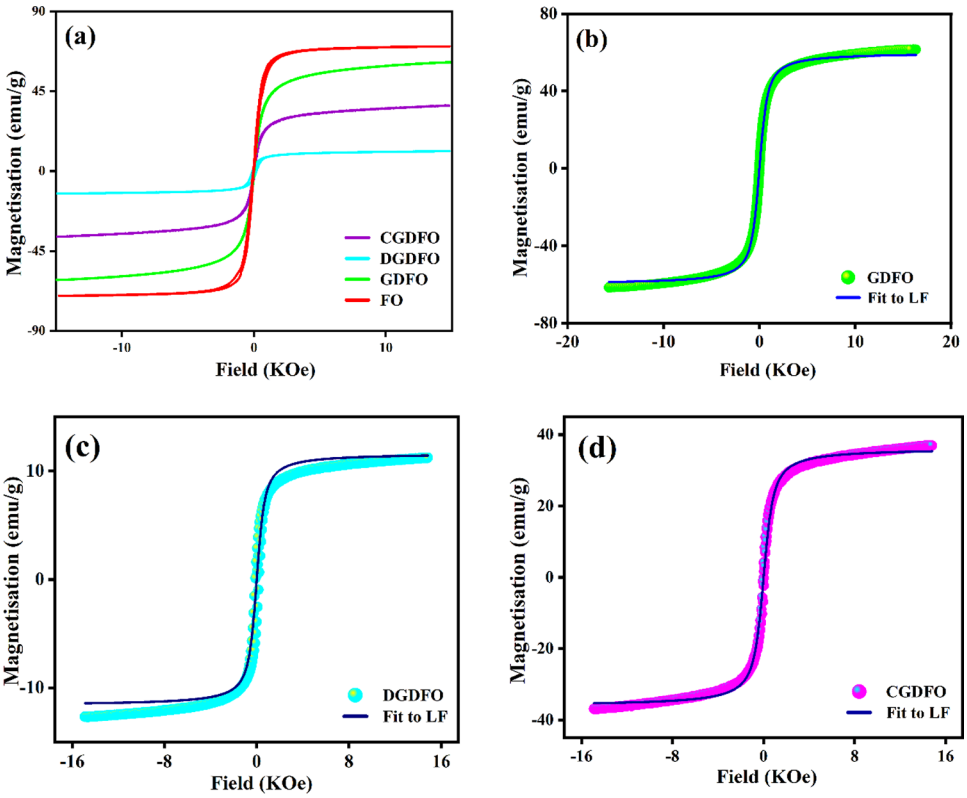

Figure 12. (a) M−H hysteresis loops of prepared MNPs and Langevin fit of (b) GdFO MNPs, (c) DGdFO MNPs, and (d) CGdFO MNPs.

Table 3. Magnetic Measurements [Saturation Magnetization (M_s), Coercivity (H_c), Retentivity (M_r), and Effective Anisotropy Constant (k_{eff})]

sample details	M_s (emu/g)	H_c (Oe)	M_r (emu/g)	$k_{eff} \times 10^5$ (erg/cm^3)
FO	70.61	22	2.59	2.59
GdFO	60.68	9	1.49	2.23
CGdFO	36.78	6	0.91	1.40
DGdFO	11.21	4	0.86	0.51

influences the tetrahedral and octahedral sites and initiates the enriching bond length compared to the bare ones.

It has been observed that the M_s value has increased in the case of CGdFO compared to DGdFO, which can be explained via ligand field theory,[45,46] as chitosan and dextran behave as a ligand and further impact the crystal field splitting. The theory of ligand field stabilization energy suggests that when a cation is under the influence of a strong field ligand, the energy of its d-orbitals splits (Δ_o), and it adopts a low spin state to achieve a stable configuration.[45,46] In the case of chitosan-coated MNPs, it has been observed that due to the domination of the amine group present in chitosan, it has a greater tendency to prefer the low spin state of Fe^{3+} in the octahedral site. On the contrary, due to the existence of a hydroxyl group in dextran-coated MNPs, it behaves as a weak field ligand with a high spin state,[45] as displayed in Figure 14. The anisotropy values (k_{eff}) for the samples doped with Gd and surface-functionalized GdFO were observed to be lower than those of the FO. In this regard, the reason for the reducing the anisotropy constant in CGdFO and DGdFO MNPs is the weak interaction between Gd−Fe which decreased the ratio of orbital to spin moments of *4f* electrons and further weakened the spin−orbit coupling.[47] The decreasing trend of coercivity (H_c) for the processed MNPs due to the lower value of the anisotropy

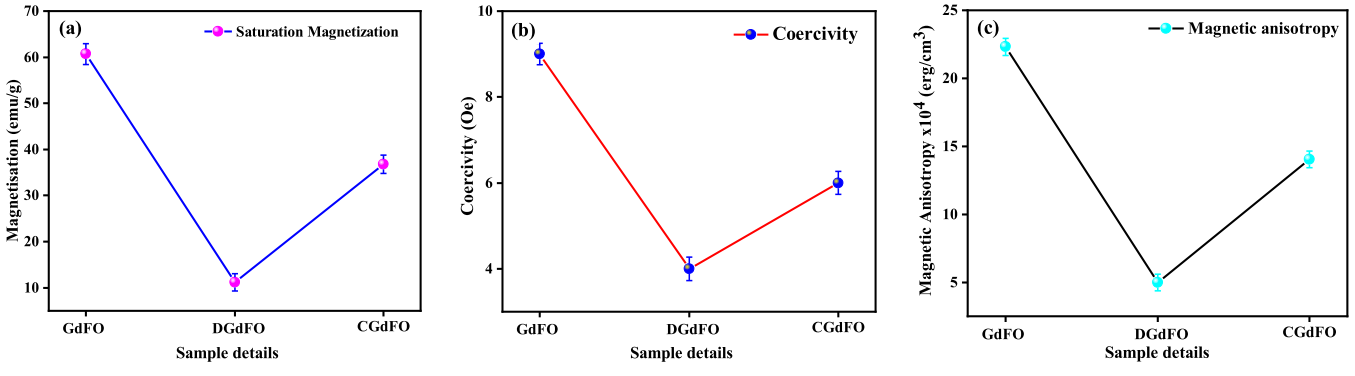

Figure 13. Variation of (a) saturation magnetization, (b) coercivity, and (c) magnetic anisotropy of the reference MNPs.

https://doi.org/10.1021/acsomega.3c07835
ACS Omega 2024, 9, 6696−6708

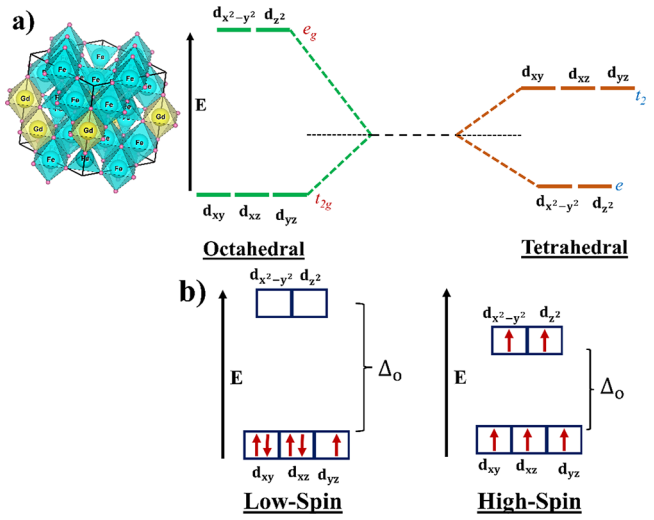

Figure 14. d^5 orbital spin arrangement of Fe^{3+} ion (a) with tetrahedral split and octahedral split and (b) octahedral split (Δ_o) under the effect of high field ligand (low spin) and weak field ligand (high spin).

constant (k_{eff}), which can be explained via Stoner–Wohlfarth model.[48]

3.4. Self-Heating Efficiency Study. To validate the applicability of the reference MNPs for hyperthermia application, their magnetic heating effect is most likely stimulated by an AC magnetic field at a frequency of 336 kHz, an alternating current of 250 A, and the magnetic field strength of 14.91 kAm^{-1}, under the clinical safety limits ($Hf \leq 5 \times 10^9$ $Am^{-1}s^{-1}$).[49] The "self-heating" of MNPs is a procedure that can produce heat by utilizing an external AC magnetic field. In the present study, highly researched Fe_3O_4 MNPs have been elected as a reference material and tried to tune its properties with appropriate Gd doping and further coating with biocompatible chitosan and dextran.[15,43,46,50] Figure 15 portrays the time-dependent temperature variant curve for processed MNPs at 1 mg/mL concentration. As indicated in Figure 15, excluding FO MNPs, all the reference NPs displayed the hyperthermic threshold regime (40–47 °C).[51] As soon as the temperature rises, it drops to a saturation regime after a specific time frame.[52,53] Overall, the ability of MNPs to generate heat is a crucial parameter in MH, and optimizing this process is essential to the success of the therapy. To do so, the heat generation capability of the MNPs can be evaluated by the Box–Lucas model to estimate the SAR and intrinsic loss power (ILP), as displayed in Figure 16.[54] Moreover, apart from moderate saturation magnetization, the controlling dipolar interaction enhances the self-heating efficiency of the dextran- and chitosan-coated Gd-doped Fe_3O_4 MNPs compared to GdFO and FO MNPs, as portrayed in Figure 16. At the outset, each MNP is probably undergoing a combination of Neel relaxation, which entails flipping its magnetic dipole moment along the easy axis, and Brownian relaxation, which involves the rotation of its entire magnetic dipole.[31,55] It is well documented that the dipole–dipole interactions between MNPs can significantly impact the SAR in MFH.[56] These interactions arise from the magnetic dipole moments of the NPs, which can align with each other in the presence of an external magnetic field.[57] Controlling dipole–dipole interactions can improve the SAR in several ways: (i) Increasing NP spacing: by increasing the spacing between NPs, the strength of the interactions can be reduced, leading to a slower relaxation time and hence a higher SAR. (ii) Orienting NP magnetic moments. The orientation of the magnetic moments of the NPs relative to each other can affect the strength of the dipole–dipole interactions. The interactions can be enhanced or weakened by aligning the moments in a specific direction depending on the desired outcome. Henceforth, understanding the role of controlling dipole–dipole interactions is essential for maximizing the SAR for MH application.[58–60]

According to Figure 17, the particle size is a crucial parameter to heat generation, as SAR varies with the size of MNPs. In vivo studies of superparamagnetic MNPs support our assumptions based on (i) NP composition and size range compliance with FDA requirements.[61] (ii) A living body can anchor NPs to target tissues so that they are unable to rotate their crystallographic axes (e.g., MNPs inside cells).[62] Additionally, the XRD and TEM analysis reveals that the particle size is in the range of ≥17 nm and SAR increases with the particle size, as depicted in Figure 17. It was found by Zubarev et al. that the intrinsic interaction of MNPs with diameters of 17–20 nm can significantly lead up to 30% higher heat production.[63] According to the magnetic analysis, MNPs are near enough to superparamagnetic, indicating that relaxation losses (Brownian and Neel relaxation losses) govern the heat generation instead of hysteresis losses.[64] Due to the control of dipolar interaction, Brownian and Neel relaxation mechanisms can withstand together, and the assumption was made that surface coating would result in a reduction of the dipole–

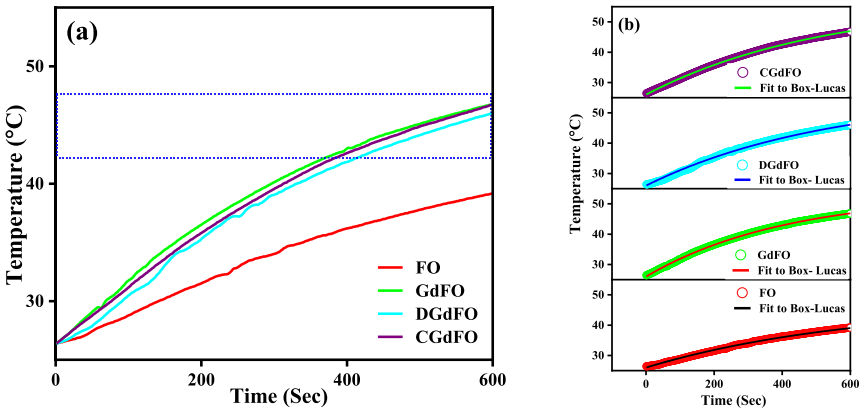

Figure 15. Time-dependent temperature deviation curve (a) for 1 mg/mL concentrations. (b) Box–Lucas fit for the synthesized MNPs.

https://doi.org/10.1021/acsomega.3c07835
ACS Omega 2024, 9, 6696–6708

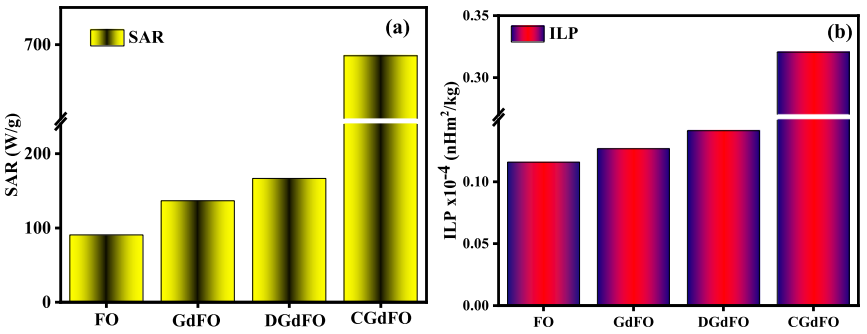

Figure 16. (a) SAR variation. (b) ILP variation with the prepared samples.

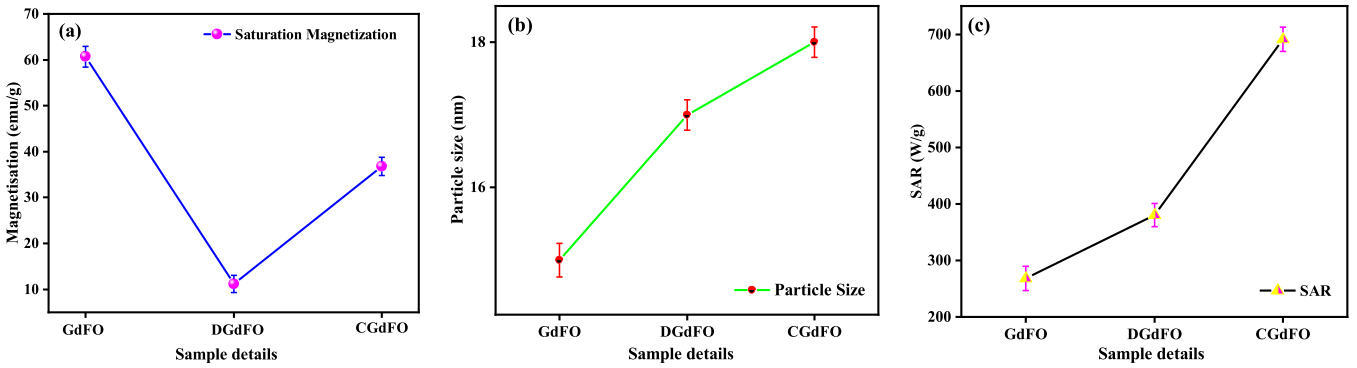

Figure 17. Variation of (a) particle size, (b) saturation magnetization, and (c) SAR of the reference MNPs.

dipole interaction strength, which in turn, resulted in a slightly higher SAR for the dextran- and chitosan-coated samples compared to the uncoated one.[65] Additionally, the surface coating of MNPs causes them to disperse and enhances the Brownian relaxation process by reducing their hydrodynamic volume, leading to an improved SAR for the coated MNPs. In this regard, the above-mentioned ESR analysis reflects the dominance of spin−spin relaxation, signifying the predominance of the controlled dipole−dipole interaction for enriching SAR in our system.[66] It has been reported that the dipolar interaction energy[67] ($\varepsilon_{Dipolar}$) per particle is $\varepsilon_{Dipolar} = \alpha\mu^2/d^3$, where α represents the proportionality constant, μ is the magnetic moment of the MNPs, and d is the mean interparticle distance. Notably, the dipolar interaction energy is directly proportional to the demagnetizing field.[68] Therefore, the existence of $\varepsilon_{Dipolar}$ induces a random torque, which perturbs the spin relaxation process by the competition between intraparticle interactions and anisotropy among the MNPs.[56] As a consequence, the competition gives rise to frustrated magnetic moments or randomization of easy anisotropy axes orientation, so a demagnetizing effect arises in the system, which may cause reduced heating efficacy in uncoated MNPs. The reduced coercivity observed in the coated samples compared to their corresponding uncoated samples can be better understood through the M−H loop analysis, as shown in Table 3. A remarkable aspect of the comparative study shows that the processed MNPs with enhanced SAR are effectively controlled over the particle size and magnetization. Henceforward, by using MNPs with a maximum SAR value, it is possible to minimize the relative dose assigned to the patient, as portrayed in Figure 14.[69] In summary, with high heating efficacy, chitosan-coated Gd-doped Fe_3O_4 MNPs can be considered a safe and effective hyperthermia agent.

4. CONCLUSIONS

In conclusion, the use of dextran- and chitosan-coated Gd-doped magnetite NPs provides a promising strategy for achieving controlled dipolar interactions for MFH applications. Incorporating Gd doping and coating with biocompatible polymers results in excellent structure, morphology, magnetic properties, and increased SAR value, making them suitable for hyperthermia applications. Furthermore, the controlled dipolar interactions between the NPs can be precisely regulated by adjusting the concentration of MNPs and the strength of the magnetic field. Additionally, self-heating efficacy for chitosan-coated Gd-doped FO MNPs directed the maximum SAR (684.99 W/g) value over all the processed samples. Therefore, there is a finite possibility for future investigations to explore the feasibility of using these MNPs in vivo and to optimize the treatment parameters for an exciting new avenue toward successful MFH applications.

■ ASSOCIATED CONTENT

Data Availability Statement

The data that support the findings of this study are available within the article.

Supporting Information

The Supporting Information is available free of charge at https://pubs.acs.org/doi/10.1021/acsomega.3c07835.

Size distribution of synthesized MNPs (PDF)

■ AUTHOR INFORMATION

Corresponding Author

J. P. Borah − *Nanomagnetism Group, Department of Physics, National Institute of Technology Nagaland, Dimapur, Nagaland 797103, India;* orcid.org/0000-0003-0086-7926; Email: jpborah@rediffmail.com

https://doi.org/10.1021/acsomega.3c07835
ACS Omega 2024, 9, 6696−6708

Authors

Krishna Priya Hazarika − *Nanomagnetism Group, Department of Physics, National Institute of Technology Nagaland, Dimapur, Nagaland 797103, India*

C. Borgohain − *Central Instrumentation Facility (CIF), Indian Institute of Technology Guwahati, Guwahati, Assam 781039, India*

Complete contact information is available at: https://pubs.acs.org/10.1021/acsomega.3c07835

Notes

The authors declare no competing financial interest.

■ ACKNOWLEDGMENTS

The authors would like to acknowledge the Central Instrument Facility (CIF), IIT Guwahati for providing all the necessary facilities required for the characterization of the samples.

■ REFERENCES

(1) Nemati, Z.; Alonso, J.; Rodrigo, I.; Das, R.; Garaio, E.; García, J. Á.; Orue, I.; Phan, M. H.; Srikanth, H. Improving the Heating Efficiency of Iron Oxide Nanoparticles by Tuning Their Shape and Size. *J. Phys. Chem. C* **2018**, *122* (4), 2367−2381.

(2) Park, J. C.; Lee, G. T.; Kim, H. K.; Sung, B.; Lee, Y.; Kim, M.; Chang, Y.; Seo, J. H. Surface Design of Eu-Doped Iron Oxide Nanoparticles for Tuning the Magnetic Relaxivity. *ACS Appl. Mater. Interfaces* **2018**, *10* (30), 25080−25089.

(3) Fantechi, E.; Innocenti, C.; Zanardelli, M.; Fittipaldi, M.; Falvo, E.; Carbo, M.; Shullani, V.; Di Cesare Mannelli, L.; Ghelardini, C.; Ferretti, A. M.; Ponti, A.; Sangregorio, C.; Ceci, P. A Smart Platform for Hyperthermia Application in Cancer Treatment: Cobalt-Doped Ferrite Nanoparticles Mineralized in Human Ferritin Cages. *ACS Nano* **2014**, *8* (5), 4705−4719.

(4) Gupta, R.; Tomar, R.; Chakraverty, S.; Sharma, D. Effect of Manganese Doping on the Hyperthermic Profile of Ferrite Nanoparticles Using Response Surface Methodology. *RSC. Advances.* **2021**, *11*, 16942−16954.

(5) Branquinho, L. C.; Carrião, M. S.; Costa, A. S.; Zufelato, N.; Sousa, M. H.; Miotto, R.; Ivkov, R.; Bakuzis, A. F. Effect of Magnetic Dipolar Interactions on Nanoparticle Heating Efficiency: Implications for Cancer Hyperthermia. *Sci. Rep.* **2013**, *3*, 20−22.

(6) Keifer, G.; Effenberger, F. *Magnetic Oxides*; Springer, 1967; Vol. *6*; pp 107−150.

(7) Nazari, M.; Ghasemi, N.; Maddah, H.; Motlagh, M. M. Synthesis and Characterization of Maghemite Nanopowders by Chemical Precipitation Method. *J. Nanostructure Chem.* **2014**, *4* (2), 2−6.

(8) Hazarika, K. P.; Borah, J. P. Biocompatible Tb Doped Fe3O4 Nanoparticles with Enhanced Heating Efficiency for Magnetic Hyperthermia Application. *J. Magn. Magn. Mater.* **2022**, *2022* (560), 251−256.

(9) Priya, K.; Fopase, R.; Pandey, L. M.; Borah, J. P. Influence of Gd-Doping on Structural, Magnetic, and Self-Heating Properties of Fe_3O_4 Nanoparticles towards Magnetic Hyperthermia Applications. *Phys. B* **2022**, *645*, No. 414237.

(10) Thakur, P.; Sharma, R.; Sharma, V.; Barman, P. B.; Kumar, M.; Barman, D.; Katyal, S. C.; Sharma, P. Gd3+ Doped Mn-Zn Soft Ferrite Nanoparticles: Superparamagnetism and Its Correlation with Other Physical Properties. *J. Magn. Magn. Mater.* **2017**, *432*, 208−217.

(11) Kadam, A. A.; Shinde, S. S.; Yadav, S. P.; Patil, P. S.; Rajpure, K. Y. Structural, Morphological, Electrical and Magnetic Properties of Dy Doped Ni-Co Substitutional Spinel Ferrite. *J. Magn. Magn. Mater.* **2013**, *329*, 59−64.

(12) Satyanarayana, S.; Sarma, S. C.; Peter, S. C.; Bhattacharya, S. Magnetic Characterization of Nano-Sized Terbium Doped Bismuth Ferrite Synthesized by Sol-Gel Method. *J. Magn. Magn. Mater.* **2019**, *491*, No. 165571.

(13) Slimani, Y.; Almessiere, M. A.; Guner, S.; Aktas, B.; Shirsath, S. E.; Silibin, M. V.; Trukhanov, A. V.; Baykal, A. Impact of Sm3+ and Er3+ Cations on the Structural, Optical, and Magnetic Traits of Spinel Cobalt Ferrite Nanoparticles: Comparison Investigation. *ACS Omega.* **2022**, *7*, 6292−6301.

(14) Naha, P. C.; Hsu, J. C.; Kim, J.; Shah, S.; Bouché, M.; Si-Mohamed, S.; Rosario-Berrios, D. N.; Douek, P.; Hajfathalian, M.; Yasini, P.; Singh, S.; Rosen, M. A.; Morgan, M. A.; Cormode, D. P. Dextran-Coated Cerium Oxide Nanoparticles: A Computed Tomography Contrast Agent for Imaging the Gastrointestinal Tract and Inflammatory Bowel Disease. *ACS Nano* **2020**, *14* (8), 10187−10197.

(15) Lachowicz, D.; Górka, W.; Kmita, A.; Bernasik, A.; Zukrowski, J.; Szczerba, W.; Sikora, M.; Kapusta, C.; Zapotoczny, S. Enhanced Hyperthermic Properties of Biocompatible Zinc Ferrite Nanoparticles with a Charged Polysaccharide Coating. *J. Mater. Chem. B* **2019**, *7* (18), 2962−2973.

(16) Shakil, M. S.; Hasan, M. A.; Uddin, M. F.; Islam, A.; Nahar, A.; Das, H.; Khan, M. N. I.; Dey, B. P.; Rokeya, B.; Hoque, S. M. In Vivo Toxicity Studies of Chitosan-Coated Cobalt Ferrite Nanocomplex for Its Application as MRI Contrast Dye. *ACS Appl. Bio Mater.* **2020**, *3* (11), 7952−7964.

(17) Corot, C.; Robert, P.; Idée, J. M.; Port, M. Recent Advances in Iron Oxide Nanocrystal Technology for Medical Imaging. *Adv. Drug Delivery Rev.* **2006**, *58* (14), 1471−1504.

(18) Oh, Y.; Lee, N.; Kang, H. W.; Oh, J. In Vitro Study on Apoptotic Cell Death by Effective Magnetic Hyperthermia with Chitosan-Coated MnFe2O4. *Nanotechnology* **2016**, *27* (11), No. 115101.

(19) Shatooti, S.; Mozaffari, M.; Reiter, G.; Zahn, D.; Dutz, S. Heat Dissipation in Sm^{3+} and Zn^{2+} Co-Substituted Magnetite ($Zn_{0.1}Sm_xFe_{2.9-X}O_4$) Nanoparticles Coated with Citric Acid and Pluronic F127 for Hyperthermia Application. *Sci. Rep.* **2021**, *11*, 16795 DOI: 10.1038/s41598-021-96238-2.

(20) Pourmortazavi, S. M.; Sahebi, H.; Zandavar, H.; Mirsadeghi, S. Fabrication of Fe3O4 Nanoparticles Coated by Extracted Shrimp Peels Chitosan as Sustainable Adsorbents for Removal of Chromium Contaminates from Wastewater: The Design of Experiment. *Compos. Part B Eng.* **2019**, *175* (2019), No. 107130.

(21) Antic, B.; Kremenovic, A.; Nikolic, A. S.; Stoiljkovic, M. Cation Distribution and Size-Strain Microstructure Analysis in Ultrafine Zn - Mn Ferrites Obtained from Acetylacetonato Complexes. *J. Phys. Chem. B* **2004**, *108* (34), 12646−12651.

(22) J, R.-C.; R, R. Line broadening analysis using fullprof: Determination. *Mater. Sci. Forum* **2004**, *444*, 123−126.

(23) Paswan, S. K.; Kumari, S.; Kar, M.; Singh, A.; Pathak, H.; Borah, J. P.; Kumar, L. Optimization of Structure-Property Relationships in Nickel Ferrite Nanoparticles Annealed at Different Temperature. *J. Phys. Chem. Solids* **2021**, *151*, No. 109928.

(24) Waldron, R. D. Infrared Spectra of Ferrites. *Phys. Rev.* **1955**, *99*, 1727−1735.

(25) Patange, S. M.; Shirsath, S. E.; Jadhav, S. P.; Hogade, V. S.; Kamble, S. R.; Jadhav, K. M. Elastic Properties of Nanocrystalline Aluminum Substituted Nickel Ferrites Prepared by Co-Precipitation Method. *J. Mol. Struct.* **2013**, *1038*, 40−44.

(26) Nam, P. H.; Phuc, N. X.; Manh, D. H.; Tung, D. K.; Nguyen, V. Q.; Nam, N. H.; Son, P. K.; Bach, T. N.; Phong, P. T. Physical Characterization and Heating Efficacy of Chitosan-Coated Cobalt Ferrite Nanoparticles for Hyperthermia Application. *Phys. E* **2021**, *134*, No. 114862.

(27) Aranaz, I.; Alcántara, A. R.; Civera, M. C.; Arias, C.; Elorza, B.; Caballero, A. H.; Acosta, N. Chitosan: An Overview of Its Properties and Applications. *Polymers* **2021**, *13* (19), 3256.

(28) Abbas, Y. M.; Mansour, A. B.; Ali, S. E.; Ibrahim, A. H. Journal of Magnetism and Magnetic Materials Investigation of Structural and Magnetic Properties of Multiferroic La 1 − x Y x FeO 3 Perovskites, Prepared by Citrate Auto-Combustion Technique. *J. Magn. Magn. Mater.* **2019**, *482* (March), 66−74.

(29) Jamir, M.; Islam, R.; Pandey, L. M.; Borah, J. P. Effect of Surface Functionalization on the Heating Efficiency of Magnetite

Nanoclusters for Hyperthermia Application. *J. Alloys Compd.* **2021**, *854*, No. 157248.
(30) Mukherjee, S.; Pal, A. K.; Bhattacharya, S.; Chattopadhyay, S. Field-Induced Spin − Flop Transitions of Interacting Nanosized α -Fe 2 O 3 Particles Dispersed in a Silica Glass Matrix. *J. Phys. Condens. MATTER* **2008**, *20*, No. 055204.
(31) Das, R.; Chaudhuri, U.; Chanda, A.; Mahendiran, R. Broadband Electron Spin Resonance Study in a Sr2FeMoO6Double Perovskite. *ACS Omega* **2020**, *5* (28), 17611−17616.
(32) Shukla, V. K.; Mukhopadhyay, S. Transverse Spin Relaxation and Magnetic Correlation in $Pr_{1-X}Ca_xMnO_3$: Inuence of Particle Size Variation and Chemical Doping. *J. Appl. Phys.* **2017**, *3*, 1−8.
(33) Vasilchikova, T.; Nalbandyan, V.; Shukaev, I.; Koo, H. J.; Whangbo, M. H.; Lozitskiy, A.; Bogaychuk, A.; Kuzmin, V.; Tagirov, M.; Vavilova, E.; Vasiliev, A.; Zvereva, E. Peculiarities of Magnetic Ordering in the S = 5/2 Two-Dimensional Square-Lattice Antimonate NaMnSb O4. *Phys. Rev. B* **2020**, *101* (5), 1−12.
(34) Lado, J. L.; Ferrón, A.; Fernández-Rossier, J. Exchange Mechanism for Electron Paramagnetic Resonance of Individual Adatoms. *Phys. Rev. B* **2017**, *96* (20), 1−6.
(35) Massoudi, J.; Smari, M.; Nouri, K.; Dhahri, E.; Khirouni, K.; Bertaina, S.; Bessais, L.; Hlil, E. K. Magnetic and Spectroscopic Properties of Ni-Zn-Al Ferrite Spinel: From the Nanoscale to Microscale. *RSC Adv.* **2020**, *10* (57), 34556−34580.
(36) Louis, N. M. Propriétés Magnétiques D Es Ferrites Ferrimagnétisme. *Ann. Phys.* **1948**, *12*, 137−198, DOI: 10.1051/anphys/194812030137.
(37) Lemine, O. M.; Madkhali, N.; Hjiri, M.; All, N. A.; Aida, M. S. Comparative Heating Efficiency of Hematite (α-Fe 2 O 3) and Nickel Ferrite Nanoparticles for Magnetic Hyperthermia Application. *Ceram. Int.* **2020**, *46* (18), 28821−28827.
(38) Gholizadeh, A. A Comparative Study of the Physical Properties of Cu-Zn Ferrites Annealed under Different Atmospheres and Temperatures: Magnetic Enhancement of Cu 0. 5 Zn 0.5 Fe 2 O 4 Nanoparticles by a Reducing Atmosphere. *J. Magn. Magn. Mater.* **2018**, *452*, 389−397.
(39) Murugesan, C.; Chandrasekaran, G. Impact of Gd3+ Substitution on the Structural, Magnetic and Electrical Properties of Cobalt Ferrite Nanoparticles. *RSC Adv.* **2015**, *5* (90), 73714−73725.
(40) Aquino, R.; Depeyrot, J.; Sousa, M. H.; Tourinho, F. A.; Dubois, E.; Perzynski, R. Magnetization Temperature Dependence and Freezing of Surface Spins in Magnetic Fluids Based on Ferrite Nanoparticles. *Phys. Rev. B - Condens. Matter Mater. Phys.* **2005**, *72* (18), 1−10.
(41) Coey, J. M. D. Noncollinear Spin Arrangement in Ultrafine Ferrimagnetic Crystallites. *Phys. Rev. Lett.* **1971**, *27* (17), 1140−1142.
(42) Dhavale, R. P.; Dhavale, R. P.; Sahoo, S. C.; Kollu, P.; Jadhav, S. U.; Patil, P. S.; Dongale, T. D.; Chougale, A. D.; Patil, P. B. Chitosan Coated Magnetic Nanoparticles as Carriers of Anticancer Drug Telmisartan: PH-Responsive Controlled Drug Release and Cytotoxicity Studies. *J. Phys. Chem. Solids* **2021**, *148*, No. 109749.
(43) Kurihara, Y.; Yokota, H.; Takahashi, M. Water-Dispersible Carboxymethyl Dextran-Coated Melamine Nanoparticles for Biosensing Applications. *ACS Omega* **2022**, *7*, 41641.
(44) Li, Q.; Kartikowati, C. W.; Horie, S.; Ogi, T.; Iwaki, T.; Okuyama, K. Correlation between Particle Size/Domain Structure and Magnetic Properties of Highly Crystalline Fe3O4 Nanoparticles. *Sci. Rep.* **2017**, *7* (1), 1−4.
(45) Trueba, A.; Aramburu, J. A.; Barriuso, M. T.; Moreno, M. Spectrochemical Series and the Dependence of Racah and 10 Dq Parameters on the Metal - Ligand Distance: Microscopic Origin. *J. Phys. Chem. A* **2011**, *2011* (115), 1423−1432.
(46) Chakraborty, I.; Majumder, D.; Rakshit, R.; Alam, M.; Mukherjee, S.; Gorai, A.; Mandal, K. Magnetic Field-Dependent Photoluminescence of Tartrate-Functionalized Gadolinium-Doped Manganese Ferrite Nanoparticles: A Potential Therapeutic Agent for Hyperbilirubinemia Treatment. *ACS Appl. Nano Mater.* **2021**, *4* (5), 4379−4387.
(47) Luo, C.; Zhang, W.; Wong, P. K. J.; Zhai, Y.; You, B.; Du, J.; Zhai, H. The Influence of Nd Dopants on Spin and Orbital Moments in Nd-Doped Permalloy Thin Films. *Appl. Phys. Lett.* **2014**, *105* (8), No. 082405.
(48) Kahmann, T.; Rösch, E. L.; Enpuku, K.; Yoshida, T.; Ludwig, F. Determination of the Effective Anisotropy Constant of Magnetic Nanoparticles − Comparison between Two Approaches. *J. Magn. Magn. Mater.* **2021**, *519*, No. 167402.
(49) Kossatz, S.; Ludwig, R.; Dähring, H.; Ettelt, V.; Rimkus, G.; Marciello, M.; Salas, G.; Patel, V.; Teran, F. J.; Hilger, I. High Therapeutic Efficiency of Magnetic Hyperthermia in Xenograft Models Achieved with Moderate Temperature Dosages in the Tumor Area. *Pharm. Res.* **2014**, *31* (12), 3274−3288.
(50) Lee, J. H.; Kim, B.; Kim, Y.; Kim, S. K. Ultra-High Rate of Temperature Increment from Superparamagnetic Nanoparticles for Highly Efficient Hyperthermia. *Sci. Rep.* **2021**, *11* (1), 1−9.
(51) Rosensweig, R. E. Heating Magnetic Fluid with Alternating Magnetic Field. *J. Urol.* **2002**, *252* (6 I), 370−374.
(52) Chalkidou, A.; Simeonidis, K.; Angelakeris, M.; Samaras, T.; Martinez-boubeta, C.; Balcells, L. Journal of Magnetism and Magnetic Materials In Vitro Application of Fe/MgO Nanoparticles as Magnetically Mediated Hyperthermia Agents for Cancer Treatment. *J. Magn. Magn. Mater.* **2011**, *323* (6), 775−780.
(53) Do, E. D.; Manna, P. K.; Nickel, R.; Van Lierop, J. Comparative Heating E Ffi Ciency of Cobalt-, Manganese-, and Nickel- Ferrite Nanoparticles for a Hyperthermia Agent in Biomedicines. *ACS Appl. Mater. Interfaces* **2019**, *2019* (11), 6858−6866.
(54) Lanier, O. L.; Korotych, O. I.; Monsalve, A. G.; Wable, D.; Savliwala, S.; Grooms, N. W. F.; Nacea, C.; Tuitt, O. R.; Lanier, O. L.; Korotych, O. I.; Monsalve, A. G.; Wable, D.; Grooms, N. W. F.; Nacea, C.; Tuitt, O. R.; Evaluation, J. D. Evaluation of Magnetic Nanoparticles for Magnetic Fluid Hyperthermia. *Int. J. Hyperth.* **2019**, *36* (1), 687−701.
(55) Dey, C. C.; Mallick, A.; Mahapatra, A. S.; Dalal, M.; Bajorek, A.; Greneche, J. M.; Ningthoujam, R. S.; Chakrabarti, P. K. Mössbauer Analysis and Induction Heating Evaluation of Grapes like FZ@ MWCNT towards Cancer Treatment. *Solid State Sci.* **2021**, *122* (April), No. 106756.
(56) Ralandinliu Kahmei, R. D.; Borah, J. P. Clustering of MnFe2O4 Nanoparticles and the Effect of Field Intensity in the Generation of Heat for Hyperthermia Application. *Nanotechnology* **2019**, *30*, No. 035706.
(57) Fu, R.; Yan, Y.; Roberts, C.; Liu, Z.; Chen, Y. The Role of Dipole Interactions in Hyperthermia Heating Colloidal Clusters of Densely-Packed Superparamagnetic Nanoparticles. *Sci. Rep.* **2018**, *8* (1), 1−10.
(58) Landi, G.; Role, T. of Dipolar Interaction in Magnetic Hyperthermia. *Phys. Rev. B - Condens. Matter Mater. Phys.* **2014**, *89* (1), 1−6.
(59) Valdés, D. P.; Lima, E.; Zysler, R. D.; Goya, G. F.; De Biasi, E. Role of Anisotropy, Frequency, and Interactions in Magnetic Hyperthermia Applications: Noninteracting Nanoparticles and Linear Chain Arrangements. *Phys. Rev. Appl.* **2021**, *15* (4), 1−18.
(60) García-Acevedo, P.; González-Gómez, M. A.; Arnosa-Prieto, Á.; de Castro-Alves, L.; Piñeiro, Y.; Rivas, J. Role of Dipolar Interactions on the Determination of the Effective Magnetic Anisotropy in Iron Oxide Nanoparticles. *Adv. Sci.* **2022**, *10*, No. 2203397, DOI: 10.1002/advs.202203397.
(61) Bobo, D.; Robinson, K. J.; Islam, J.; Thurecht, K. J.; Corrie, S. R. Nanoparticle-Based Medicines: A Review of FDA-Approved Materials and Clinical Trials to Date. *Pharm. Res.* **2016**, *33* (10), 2373−2387.
(62) Di Corato, R.; Espinosa, A.; Lartigue, L.; Tharaud, M.; Chat, S.; Pellegrino, T.; Ménager, C.; Gazeau, F.; Wilhelm, C. Magnetic Hyperthermia Efficiency in the Cellular Environment for Different Nanoparticle Designs. *Biomaterials* **2014**, *35* (24), 6400−6411.
(63) Zubarev, A. Y. Magnetic Hyperthermia in a System of Immobilized Magnetically Interacting Particles. *Phys. Rev. E* **2019**, *99* (6), 1−6.

https://doi.org/10.1021/acsomega.3c07835
ACS Omega 2024, 9, 6696−6708

(64) Lima, E.; Torres, T. E.; Rossi, L. M.; Rechenberg, H. R.; Berquo, T. S.; Ibarra, A.; Marquina, C.; Ibarra, M. R.; Goya, G. F. Size Dependence of the Magnetic Relaxation and Specific Power Absorption in Iron Oxide Nanoparticles. *J. Nanoparticle Res.* **2013**, *15* (5), 1654.
(65) Arteaga-Cardona, F.; Rojas-Rojas, K.; Costo, R.; Mendez-Rojas, M. A.; Hernando, A.; de la Presaa, P. Improving the Magnetic Heating by Disaggregating Nanoparticles. *J. Alloys Compd.* **2016**, *663*, 636−644.
(66) Hergt, R.; Dutz, S.; Zeisberger, M. Validity Limits of the Néel Relaxation Model of Magnetic Nanoparticles for Hyperthermia. *Nanotechnology* **2010**, *21* (1), No. 015706.
(67) Allia, P.; Coisson, M.; Tiberto, P.; Vinai, F.; Knobel, M.; Novak, M. A.; Nunes, W. C. Granular Cu-Co Alloys as Interacting Superparamagnets. *Phys. Rev. B - Condens. Matter Mater. Phys.* **2001**, *64* (14), 1444201−14442012.
(68) Held, G. A.; Grinstein, G.; Doyle, H.; Sun, S.; Murray, C. B. Competing Interactions in Dispersions of Superparamagnetic Nanoparticles. *Phys. Rev. B - Condens. Matter Mater. Phys.* **2001**, *64* (1), 124081−124084.
(69) Sharma, S. K.; Shrivastava, N.; Rossi, F.; Le Duc, T.; Thi Kim Thanh, N. Nanoparticles-Based Magnetic and Photo Induced Hyperthermia for Cancer Treatment. *Nano Today* **2019**, 1−4.

https://doi.org/10.1021/acsomega.3c07835
ACS Omega 2024, 9, 6696−6708